Numerical simulation of the Zeeman effect in neutral xenon from NIR diode-laser spectroscopy

Baïlo B. Ngom,[a] Timothy B. Smith, Wensheng Huang, and Alec D. Gallimore
Department of Aerospace Engineering, University of Michigan, Ann Arbor, Michigan 48109, USA

(Received 7 January 2008; accepted 7 May 2008; published online 23 July 2008)

We present a numerical method for simulating neutral xenon absorption spectra from diode-laser spectroscopy of the Zeeman-split $6S'[1/2] \rightarrow 6P'[1/2]$ line at 834.682 nm-air in a galvatron's plasma. To simulate the spectrum, we apply a Voigt profile to a spectrum of σ-transition lines of even- and odd-numbered isotopes computed from anomalous Zeeman and nonlinear Zeeman hyperfine structure theories, respectively. Simulated spectra agree well with Zeeman-split spectra measured from 30 to 300 G. A commercial nonlinear least-squares solver (LSQNONLIN) returns field strengths and translational plasma kinetic temperatures that minimize the error between simulated and experimental spectra. This work is a preamble to computing magnetic field topology and the speed distribution of neutral xenon particles in the plume of a Hall thruster from diode laser-induced fluorescence. © *2008 American Institute of Physics*. [DOI: 10.1063/1.2955761]

I. INTRODUCTION

Understanding the interaction between circuit-induced magnetic fields and plasma discharges in Hall thrusters is key to improving lifetime and performance.[1,2] Studies of the magnetic field topology in the plumes of such thrusters have thus far relied on software-based modeling and physical probe-based measurements. Both these methods have limited field-mapping capabilities. In the former, magnetic fields are modeled in the vacuum environment of a "cold" thruster in which only coil currents generate the magnetic field. When combined with Hall or B-dot probing, vacuum field simulations do, to a certain extent, render possible the determination of Hall and beam current effects on the vacuum magnetic field. However, physical probe measurements are inherently intrusive. Perturbations from physical probe insertion include Hall current blockage, secondary electron emission, and sputtering of exposed metals and ceramics.[1,3] Probe-size reduction (often to sub-millimeter magnitudes) is typically the main recourse to reducing intrusiveness; this, however, comes at the expense of higher sensitivity to failure.

Laser-induced fluorescence (LIF) is growing increasingly popular as a reliable diagnostic tool for measuring ion and neutral velocity distributions in thruster discharges and plumes. The nonintrusive nature of this optical technique also makes it attractive for sketching the magnetic field topology in thruster discharges through spectral analysis. When subject to the external effect of field-generating thruster-magnets, energy levels of plasma-discharge particles split, thereby affecting LIF spectra. In this work, we apply an exact nonlinear model to study the Zeeman effect of the hyperfine structure of neutral xenon (Xe I) by simulating the effect of an external magnetic field on absorption spectra as Xe I particles are excited by a near infrared diode-laser beam polarized perpendicularly with respect to the field direction. In anticipation of Hall thruster LIF data exhibiting Zeeman splitting, we limit this preliminary work to optogalvanic spectra as the galvatron is immersed in the magnetic field of a Helmholtz coil. Successful spectral data fitting of the model prompted the development of a magnetic field intensity and kinetic temperature solver, which we validate in this work using optogalvanic spectra measurements at various field intensity levels spanning 30 to 300 G—a practical intensity range reflecting field magnitudes in Hall thrusters.[1,3]

II. THE ANOMALOUS ZEEMAN EFFECT

We start our theoretical introduction with the simplest Zeeman effect described by the anomalous Zeeman theory.[4] This theory applies to atoms that possess no nuclear spin and are subject to an external magnetic field of strength H. Based on the vector model, the application of such a field leads to a precession of an outer-electron's resultant momentum vector $(\vec{J})$ about the field direction $(\vec{H})$. The angle between $\vec{J}$ and $\vec{H}$ only assumes discrete values. To each possible orientation of $\vec{J}$ is associated a specific magnetic moment μ_J proportional to a quantum number M_J, whose possible values obey the rules

$$-J \leq M_J \leq J \quad \text{with} \quad \Delta M_J = 0, \pm 1. \tag{2.1}$$

This quantization of the magnetic moment leads to quantized M_J levels symmetrically distributed about each parent J level. Possible energy displacements about some parent J level for each M_J are given by

$$\Delta E = g_J M_J H. \tag{2.2}$$

When light—of a polarization vector oriented perpendicular or parallel to $\vec{H}$—excites an atom at some energy level M_J, there is a finite probability that it transits to a different energy level. The transition probability from a parent J level to a parent $J+1$ level (termed $J \rightarrow J+1$) is given by the following formulas[5] for radiation of circular polarization:

[a]Electronic mail: bbahn@umich.edu.

$$I_{M_J \to M_J - 1} = K(J - M_J + 1)(J - M_J + 2), \tag{2.3a}$$

$$I_{M_J \to M_J + 1} = K(J + M_J + 1)(J + M_J + 2), \tag{2.3b}$$

where K is an arbitrary normalization factor and all quantum numbers are associated with upper (initial) states.

III. THE ZEEMAN EFFECT OF HYPERFINE STRUCTURE

The Zeeman effect on species whose nuclear spin is nonzero—hence exhibiting hyperfine structure—is more complex due to coupled interactions of the magnetic field with momenta associated with the nucleus and an outer-electron. A matrix-based nonlinear theory[6] developed by Sommerfeld, Heisenberg, Landé, and Pauli in the 1930s accurately models the Zeeman effect on a spinning spherical body orbiting another spinning body, which induces a central force-field while an external magnetic field acts upon the overall system. A relatively simpler formulation of the theory can be found from Darwin's analysis of the problem based on wave mechanics.[6,7] In that decade, Bacher[8] applied the theory to thallium and bismuth lines in the 300–500 nm range and validated it to good approximation against observed spectra. Though useful, the theory has been, for the most part, ignored among the engineering community; this may be due to the complex nature of computations involved—especially when applied to elements with high momentum quantum numbers. As a recourse, a common trend has been to use approximate methods suited for low and high magnetic field strengths; low-field linear Zeeman and high-field Paschen-Back models are two such examples.

However, with modern advances in computing capabilities, the nonlinear Zeeman effect of hyperfine structure (ZHFS) has grown increasingly attractive for modeling spectra. As a preamble to describing the nonlinear ZHFS theory, we begin with a brief introduction of approximate models.

A. Linear Zeeman theories of hyperfine structure in weak- and strong-field strength regimes

Low- and high-field approximations of the Zeeman effect of hyperfine structure are linear theories, more thoroughly discussed by Haken *et al.*[4] and Sobelman.[5] In the present work, we only report essentials of the theories needed for a basic understanding and implementation of the nonlinear ZHFS. The weak-field Zeeman theory of hyperfine structure is applicable when the mean separation of energy levels due to hyperfine structure alone (ΔE_{hfs} as $H \to 0$) is much larger than their mean splitting arising from the Zeeman effect ΔE_{mag}. In the vector representation, the model predicts a precession of the resultant angular momentum ($\vec{F}$ resulting from IJ coupling) of an atom about $\vec{H}$. This precessive motion (which only occurs at discrete angles) leads to a quantized magnetic moment μ_M proportional to a quantum number M. The following selection rules dictate permissible values of F and M, respectively:

$$|I - J| \le F \le I + J \quad \text{with} \quad \Delta F = 0, \pm 1, \tag{3.1}$$

$$-F \le M \le F \quad \text{with} \quad \Delta M = 0, \pm 1. \tag{3.2}$$

Energy displacements about some parent F level due to an external field of strength H are given by

$$\Delta E = \mu_M H = (g_F \mu_B M) H, \tag{3.3}$$

where the Landé factor, g_F, linearly depends on electronic and nuclear Landé g-factors, g_J and g_I, respectively, as expressed below:

$$g_F = g_J \frac{F(F+1) + J(J+1) - I(I+1)}{2F(F+1)} - g_I \frac{\left(\frac{\mu_N}{\mu_B}\right)[F(F+1) - J(J+1) + I(I+1)]}{2\frac{F}{F1+1}}. \tag{3.4}$$

In Eq. (3.4), μ_B and μ_N respectively stand for Bohr magneton and nuclear magnetic moment.

In the weak-field approximation, intensities of transition lines arising from circularly polarized exciting radiation are of the same form as those given in anomalous Zeeman theory (2.3); these are found by replacing J by F and M_J by M based on Sobelman's argument that F components split in a similar fashion as the splitting of J components in a weak field.[5]

In the strong-field limit[4,8] ($\Delta E_{mag} \gg \Delta E_{hfs}$), the Paschen-Back effect of hyperfine structure applies. In this case, H is so large as to decouple the interaction between $\vec{I}$ and $\vec{J}$, leading to independent precessions of the latter vectors about $\vec{H}$. The precessions lead to separate quantized magnetic moments μ_{M_J} and μ_{M_I} respectively proportional to moment quantum numbers M_J and M_I, whose selection rules are respectively given in Eq. (2.1) and by

$$-I \le M_I \le I \quad \text{with} \quad \Delta M_I = 0, \pm 1. \tag{3.5}$$

B. Nonlinear Zeeman effect of hyperfine structure

The nonlinear theory of the Zeeman effect of hyperfine structure is based upon a simple two-particle model. A spinning particle induces a central force field on a spinning spherical particle in orbit about the former as a magnetic field externally acts upon the overall system.[6,8] The theory is exact over an arbitrarily broad range of field strengths when applied to one-electron atoms whose nuclei exert a spherically symmetric electric potential on electrons. For this physical model, the system's wave-function $\Psi = \Psi(\lambda, \chi, \mu, r, \theta, \varphi)$ is separable into respective nuclear and outer-electron components ($\Psi_N = \Psi_N(\lambda, \chi, \mu)$) and ($\Psi_E = \Psi_E(r, \theta, \varphi)$), each described in independent Eulerian polar coordinate systems.[8] Under these assumptions, the time-independent Schrödinger wave-equation assumes the form[9]

$$(V_{KE} + V_E + V_{LS} + V_{IJ} + V_H + V_{H^2})\Psi = E\Psi, \tag{3.6}$$

where the left-hand side of the equation consists of a Hamiltonian operator, which acts on the wave-function and accounts for

- kinetic energy (V_{KE}), Coulomb interaction (V_E), and electronic spin-to-angular momentum interactions (V_{LS}) responsible for fine structure;
- nuclear spin and outer-electron's resultant angular momentum interactions (V_{IJ}) responsible for hyperfine structure; and
- independent and coupled interactions of $\vec{I}$ and $\vec{J}$ with $\vec{H}$ responsible for linear (through V_H) and nonlinear (through V_{H^2}) Zeeman effects of hyperfine structure.

Solving Eq. (3.6) results in the following exact solution:[8]

$$\Psi^{M_J,M_I}(\lambda,\chi,\mu,r,\theta,\varphi) = \sum_{M_J,M_I} X_{M_J,M_I}\Psi_E^{M_J}(r,\theta,\varphi)\Psi_N^{M_I}(\lambda,\chi,\mu), \tag{3.7}$$

in which the separate electron and nuclear wave-functions take on the respective forms

$$\Psi_E^{M_J}(r,\theta,\varphi) = f(r)P_J^{M_J}(\cos\theta)e^{iM_J\varphi}, \tag{3.8a}$$

$$\Psi_N^{M_I}(\lambda,\chi,\mu) = P_I^{M_I}(\cos\chi)e^{i(M_I\lambda+\tau\mu)}. \tag{3.8b}$$

Substitution of Eqs. (3.8a) and (3.8b) into Eq. (3.7), then into the Schrödinger Eq. (3.6), and integration over the space enclosing outer-electron and nucleus subspaces leads to the following characteristic Eq. (3.9) relating each energy level to a set of up to three nonzero probability amplitudes (X) associated with each quantum state:

$$-\left[\frac{a}{2}(J-M_J+1)(I+M_I+1)\right]X_{M_J-1,M_I+1} - \left[\frac{a}{2}(J+M_J+1)(I-M_I+1)\right]X_{M_J+1,M_I-1} + [E_{M_J,M_I} - aM_JM_I - (M_Jg_J+M_Ig_I)\text{oH}]X_{M_J,M_I} = 0. \tag{3.9}$$

In the above characteristic equation, H denotes the magnetic field strength; $o=e/(4\pi mc^2)$ is the Larmor precession frequency; g_J and g_I denote Landé g-factors respectively associated with the outer-electron and the nucleus; a denotes the hyperfine unit interval; and M_J and M_I are moment quantum numbers associated with precessions of the resultant orbital momentum of the outer-electron and the spin of the nucleus about $\vec{H}$. Together with the sum rule ($M=M_J+M_I$), the selection rules of Eqs. (2.1) and (3.5) yield all permissible sets (M_J,M_I). While M is a quantum number in the weak-field approximation[10] [recall Eq. (3.1)], it is not considered as such in the nonlinear ZHFS model;[8] hence, the set $|JFM_JM_I\rangle$ is sufficient and necessary to fully describe a quantum state. To each such set corresponds a single subequation of Eq. (3.9). Considering n possible energy states, one can conveniently express the characteristic equation in matrix form as

$$[X]_{n\times n}[E]_{n\times n} = [C]_{n\times n}[X]_{n\times n}, \tag{3.10}$$

where

- $[E]$ is a diagonal square matrix whose diagonal entries consist of all possible energy displacements about some parent J level of interest;
- $[X]$ is a square matrix consisting of vectors whose components form a set of mode shape amplitudes $X_{M_J,M_I}^{J,F}$ (at most three of which are nonzero) associated with each state; and
- $[C]$ is a square matrix of factors multiplying each mode shape amplitude in Eq. (3.9).

Depending on the polarization of exciting radiation, transitions obey the following rules: $\Delta M=0$ for parallel polarization (π) and $\Delta M=\pm 1$ for circular polarization ($\sigma^{\pm}$). In this paper, we restrict our interest to the latter type of polarization for the particular class of $J\rightarrow J-1$ transitions, whose intensity formulas read

$$I = \frac{[\sum_M X_{M_J,M_I}^{J,F}X_{M_J\pm1,M_I}^{J-1,F'}(I+M_I)!\,(I-M_I)!\,(J+M_J)!\,(J-M_J)!]^2}{N_M^{J,F}N_{M\pm1}^{J-1,F}}, \tag{3.11}$$

where upper and lower state normalization constants ($N_M^{J,F}$ and $N_{M\pm1}^{J-1,F}$, respectively) are found from the formula

$$N_M^{J,F} = \sum_M (X_{M_J,M_I}^{J,F})^2(I+M_I)!\,(I-M_I)!\,(J+M_J)!\,(J-M_J)!. \tag{3.12}$$

The summations in Eqs. (3.11) and (3.12) are performed over all possible sets (M_J,M_I), satisfying the conservation of momentum condition (or sum rule): $M=M_J+M_I$. For a better grasp on the proper implementation of the above intensity formulas, we recommend the work of Bacher[8] and Darwin[7] containing several examples worked out in great detail.

IV. MODELING OF THE 834.682 NM-AIR NEUTRAL XENON (XE I) ABSORPTION SPECTRUM

Since the nine stable isotopes of xenon are atoms of zero and nonzero nuclear spin, modeling the 834.682 nm absorption spectrum of Xe I requires a different approach for each set.

A. Transition line spectra modeling of isotopes with nonzero nuclear spin

As we noted in Sec. III B, the nonlinear Zeeman theory was developed for hydrogenlike elements. However, as the ground state configuration of neutral xenon ($[Kr]4d^{10}5s^25p^6$)

suggests, this atom has many electrons. So, before applying the nonlinear ZHFS model to the two isotopes of nonzero spin (^{129}Xe and ^{131}Xe), we first ensure that our approach is reasonable. The 834.682 nm line of Xe I results from the interaction of two excited upper and lower states: $5p^5(^2P_{1/2})6s$ and $5p^5(^2P_{1/2})6p$, respectively. In this transition, a single electron from the outer $6s$ subshell assumes a higher orbital angular momentum state $6p$. The term $5p^5$ means that the outermost subshell of the ground state is vacant by one electron (since a filled p-subshell contains six electrons). This leaves the atomic system with an inner core: $[Kr]4d^{10}5s^25p^5$.[11]

The electron outside this inner core (termed "outer-electron") undergoes LK coupling[11] (also termed LS_1). In this electronic configuration scheme, L accounts for the coupling of the orbital angular momentum of the core electrons with that of the outer-electron. The interaction of L with the overall spin of core electrons leads to a resultant angular momentum K. In turn, the interaction of K and the spin of the outer-electron (S) results in an effective resultant momentum quantum number, J, associated with the outer-electron. The nomenclature in LK coupling is of the form $^{2S+1}[K]_J$, which is analogous to the naming convention of hydrogenlike atoms: nl^2L_J.[11] This analogy makes it reasonable to approximate our multi-electron atomic system as a hypothetical one-electron atomic system of orbital angular momentum K, multiplicity $2S+1$, and resultant angular momentum J.

Next, we verify the validity of the spherically symmetric nuclear field assumption for the $6S'[1/2]1 \rightarrow 6P'[3/2]1$ transition of Xe I. Aside from the main coulomb potential associated with all nuclei, there may be a differential electrostatic potential associated with nuclei of asymmetric structure.[12] This asymmetry leads to a variation of the gradient of the electric potential across the nucleus' volume, which, in turn, induces an electric quadrupole interaction moment Q. Positive and negative values of Q correspond to prolate ("cigarlike") and oblate ("disklike") structures of the nucleus, respectively. The effect of this interaction on each hyperfine structure line component is a specific shift proportional to an electric quadrupole interaction constant B given by

$$B = \frac{e^2}{4\pi\epsilon_0} q_J Q, \tag{4.1}$$

where the quantity q_J linearly depends on the electric field gradient. All nuclei of Xe I isotopes are symmetric except that of ^{131}Xe with a prolate structure ($Q>0$). Suzuki[13] provides upper- and lower-state B values for the latter isotope. When accounted for, this parameter induces shifts of hyperfine line components smaller than 5% based on transition energy formulas given by Svanberg[12]—who also reports transition intensity formulas. This is illustrated in Fig. 1(a), which compares ^{131}Xe cold spectra for $B=0$ and $B\neq 0$. Furthermore, these deviations are much less noticeable on the combined cold spectra of all isotopes [refer to Fig. 1(b)]. These facts validate the spherically symmetric potential as-

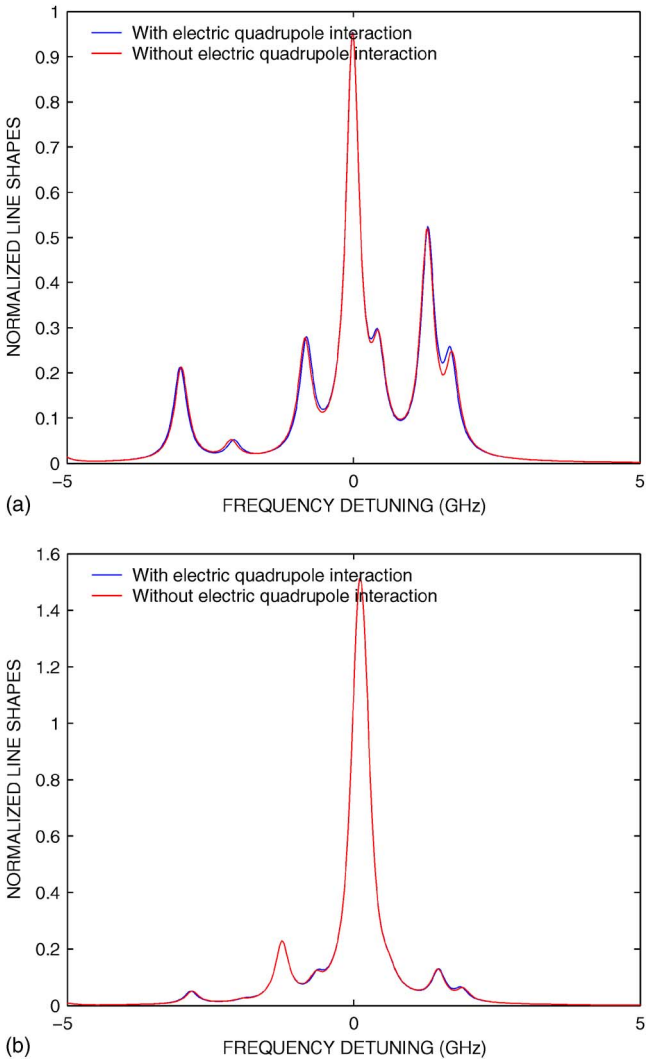

FIG. 1. (Color online) Illustration of the negligible effect of the electric quadrupole interaction on the spectrum of Xe I. (a) Effect on ^{131}Xe spectrum (isotope shift not accounted for). (b) Effect on combination of all isotopes' spectra (isotope shifts accounted for).

TABLE I. ^{129}Xe upper state's ($6S'[1/2]1$) energy levels along with corresponding unnormalized mode-shape amplitudes.

State	Energy (GHz)	Mode-shape amplitudes $X^{1,3/2}_{1,1/2}$	$X^{1,3/2}_{0,1/2}$	$X^{1,1/2}_{1,-1/2}$	$X^{1,3/2}_{-1,1/2}$	$X^{1,1/2}_{0,-1/2}$	$X^{1,3/2}_{-1,-1/2}$
$\vert 1\frac{3}{2}1\frac{1}{2}\rangle$	−2.32	1	-	-	-	-	-
$\vert 1\frac{3}{2}0\frac{1}{2}\rangle$	−2.72	-	−1	0.936	-	-	-
$\vert 1\frac{1}{2}1-\frac{1}{2}\rangle$	6.20	-	−0.468	−1	-	-	-
$\vert 1\frac{3}{2}-1\frac{1}{2}\rangle$	−3.11	-	-	-	0.535	0.934	-
$\vert 1\frac{1}{2}0-\frac{1}{2}\rangle$	5.42	-	-	-	1	−1	-
$\vert 1\frac{3}{2}-1-\frac{1}{2}\rangle$	−3.49	-	-	-	-	-	1

TABLE II. ^{129}Xe lower state's $(6P'[3/2]1)$ energy levels.

State	$\|2_{\frac{5}{2}}2_{\frac{1}{2}}\rangle$	$\|2_{\frac{5}{2}}1_{\frac{1}{2}}\rangle$	$\|2_{\frac{3}{2}}2_{-\frac{1}{2}}\rangle$	$\|2_{\frac{5}{2}}0_{\frac{1}{2}}\rangle$	$\|2_{\frac{3}{2}}1_{-\frac{1}{2}}\rangle$	$\|2_{\frac{5}{2}}-1_{\frac{1}{2}}\rangle$	$\|2_{\frac{3}{2}}0_{-\frac{1}{2}}\rangle$	$\|2_{\frac{5}{2}}-2_{\frac{1}{2}}\rangle$	$\|2_{\frac{3}{2}}-1_{-\frac{1}{2}}\rangle$	$\|2_{\frac{5}{2}}-2_{-\frac{1}{2}}\rangle$
Label	$\|1\rangle$	$\|2\rangle$	$\|3\rangle$	$\|4\rangle$	$\|5\rangle$	$\|6\rangle$	$\|7\rangle$	$\|8\rangle$	$\|9\rangle$	$\|10\rangle$
Energy (GHz)	−1.84	−2.27	−5.29	−2.69	4.67	−3.11	4.04	−3.53	3.40	−3.95

sumption necessary for the application of the nonlinear ZHFS theory in modeling the Zeeman effect of the $6S'[1/2]1 \rightarrow 6P'[3/2]1$ line of Xe I.

The application of the ZHFS theory to the $6S'[1/2] \rightarrow 6P'[3/2]$ transition of neutral isotopes ^{129}Xe (nuclear spin 1/2) and ^{131}Xe (nuclear spin 3/2) (Ref. 14) begins with the determination of lower and upper energy levels and mode-shape amplitudes based on characteristic Eq. (3.9). The fortunate fact that all physical parameters associated with the two isotopes are known for this transition renders any numerical evaluation of Eq. (3.9) trivial. Electronic Landé factors, g_J, are given by Saloman.[15] Nuclear Landé factors, g_I, can be deduced for each isotope from nuclear moments, μ_N, reported by Emsley[16] based on the relationship $g_I=(\mu_N/I)\times(m_e/m_p)$.[4] Upper and lower level hyperfine constants a are listed in Refs. 13 and 17.

As a practical illustration of the determination of energy levels from nonlinear ZHFS theory, we consider the simpler case of $6S'[1/2]1$ of ^{129}Xe for which $J=1$.[18] Starting with selection rules (3.1), (2.1), and (3.5), we find

$$F=\frac{1}{2},\frac{3}{2}; \quad M_J=0,\pm 1; \quad \text{and} \quad M_I=\pm\frac{1}{2}.$$

Next, we find all permissible combinations of M_J and M_I such that $M=M_J+M_I$, where M sums are given by Eq. (3.2). The simple process, illustrated below, leads to six possible states for $6S'[1/2]1$:

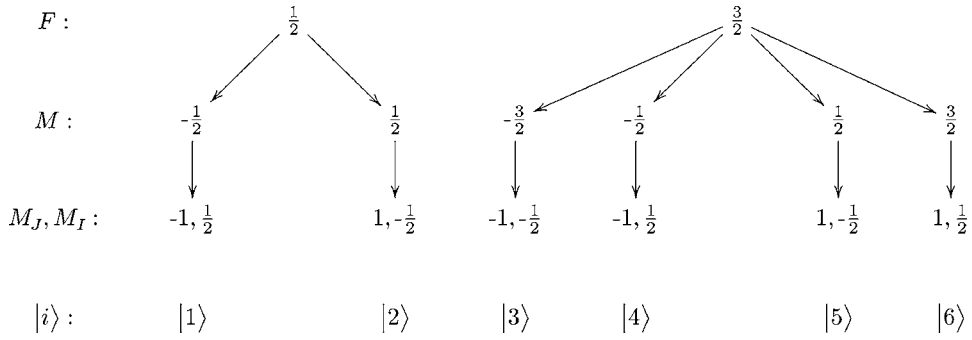

14

From the sets (M_J,M_I), we write the eigenvalue problem[19] using Eq. (3.9) in terms of some ith eigenvector associated with a state $|i\rangle$; for $H=312$ G, we express the eigenvalue problem in the following equation:

$$\left\{E^{|i\rangle}[I]-\begin{bmatrix} -2.32 & 0 & 0 & 0 & 0 & 0 \\ 0 & -1.87\times10^{-4} & -5.80 & 0 & 0 & 0 \\ 0 & -2.90 & 3.49 & 0 & 0 & 0 \\ 0 & 0 & 0 & 2.32 & -2.90 & 0 \\ 0 & 0 & 0 & -5.80 & 1.87\times10^{-4} & 0 \\ 0 & 0 & 0 & 0 & 0 & -3.49 \end{bmatrix}\right\}\begin{bmatrix} X^{1,3/2}_{1,1/2} \\ X^{1,3/2}_{0,1/2} \\ X^{1,1/2}_{1,-1/2} \\ X^{1,3/2}_{-1,1/2} \\ X^{1,1/2}_{0,-1/2} \\ X^{1,3/2}_{-1,-1/2} \end{bmatrix}=[0]. \tag{4.2}$$

TABLE III. ^{131}Xe upper state's $(6S'[1/2]1)$ energy levels.

State	$\|1_{\frac{5}{2}}1_{\frac{3}{2}}\rangle$	$\|1_{\frac{5}{2}}0_{\frac{3}{2}}\rangle$	$\|1_{\frac{3}{2}}1_{\frac{1}{2}}\rangle$	$\|1_{\frac{3}{2}}0_{\frac{1}{2}}\rangle$	$\|1_{\frac{3}{2}}0_{\frac{1}{2}}\rangle$	$\|1_{\frac{1}{2}}1_{-\frac{1}{2}}\rangle$	$\|1_{\frac{5}{2}}-1_{\frac{1}{2}}\rangle$	$\|1_{\frac{3}{2}}0_{-\frac{1}{2}}\rangle$	$\|1_{\frac{1}{2}}1_{-\frac{3}{2}}\rangle$	$\|1_{\frac{5}{2}}-1_{-\frac{1}{2}}\rangle$	$\|1_{\frac{3}{2}}0_{-\frac{3}{2}}\rangle$	$\|1_{\frac{5}{2}}-1_{-\frac{3}{2}}\rangle$
Label	$\|1\rangle$	$\|2\rangle$	$\|3\rangle$	$\|4\rangle$	$\|5\rangle$	$\|6\rangle$	$\|7\rangle$	$\|8\rangle$	$\|9\rangle$	$\|10\rangle$	$\|11\rangle$	$\|12\rangle$
Energy (GHz)	3.16	−1.50	2.94	−4.56	−1.60	2.72	−4.18	−1.75	2.49	−1.97	2.25	1.99

TABLE IV. ^{131}Xe lower state's $(6P'[3/2]1)$ energy levels.

State	$\|2_2^7 2_{\frac{3}{2}}^3\rangle$	$\|2_2^7 1_{\frac{3}{2}}^3\rangle$	$\|2_2^5 2_{\frac{1}{2}}^1\rangle$	$\|2_2^7 0_{\frac{3}{2}}^3\rangle$	$\|2_2^5 1_{\frac{1}{2}}^1\rangle$	$\|2_2^3 2_{-\frac{1}{2}}^3\rangle$	$\|2_2^7 -1_{\frac{3}{2}}^3\rangle$	$\|2_2^5 0_{\frac{1}{2}}^3\rangle$	$\|2_2^3 1_{-\frac{1}{2}}^1\rangle$	$\|2_2^1 2_{-\frac{3}{2}}^3\rangle$	$\|2_2^7 -2_{\frac{3}{2}}^3\rangle$	$\|2_2^5 -1_{\frac{1}{2}}^1\rangle$	$\|2_2^3 0_{-\frac{1}{2}}^1\rangle$	$\|2_2^1 1_{-\frac{3}{2}}^3\rangle$	$\|2_2^7 -2_{\frac{1}{2}}^1\rangle$	$\|2_2^3 0_{-\frac{3}{2}}^3\rangle$	$\|2_2^7 -2_{\frac{1}{2}}^1\rangle$	$\|2_2^5 -1_{-\frac{3}{2}}^3\rangle$	$\|2_2^7 -2_{-\frac{3}{2}}^3\rangle$
Label	$\|1\rangle$	$\|2\rangle$	$\|3\rangle$	$\|4\rangle$	$\|5\rangle$	$\|6\rangle$	$\|7\rangle$	$\|8\rangle$	$\|9\rangle$	$\|10\rangle$	$\|11\rangle$	$\|12\rangle$	$\|13\rangle$	$\|14\rangle$	$\|15\rangle$	$\|16\rangle$	$\|17\rangle$	$\|18\rangle$	$\|19\rangle$	$\|20\rangle$
Energy (GHz)	3.62	0.375	3.34	−2.01	0.105	3.06	−3.57	−0.223	−0.197	2.76	−4.54	−2.72	−0.532	2.46	−3.27	−0.894	2.15	1.28	1.84	1.52

The resulting eigenvalues (energy levels) and eigenvectors (mode shape amplitudes) are reported in Table I. For the lower state $(6P'[3/2]1)$, the eigenvalue problem is more complex in that the square coefficient matrix is ten-dimensional; the resulting energy levels are listed in Table II. The degree of complexity increases for ^{131}Xe due to a higher nuclear spin for this isotope $(I=3/2)$. The resulting 12 upper-states and 20 lower-states associated with the latter isotope are reported in Tables III and IV, respectively.

The next step in modeling the full spectrum consists of determining all allowed transitions and corresponding normalized line strengths associated with isotopes ^{129}Xe and ^{131}Xe based on transition rules and intensity and normalization formulas in Eqs. (3.11) and (3.12),[20] respectively. Table V illustrates details of the calculation of line intensities for the eleven $M \rightarrow M-1$ transitions of ^{129}Xe at $H=312$ G; expressions of unnormalized intensities[20] [numerator of Eq. (3.11)] and normalization factors from Eq. (3.12) are listed therein in terms of mode shape amplitudes. The resulting normalized intensities are also listed along with corresponding transition energies. The complete σ line spectra of the two isotopes are reported in Figs. 2 and 3.

Next, we account for the relative frequency shifts[13] and natural abundances[14] associated with each isotope. Each set of line components associated with each isotope undergoes a particular shift arising from two effects: a mass effect due to differences in the number of neutrons and a volume effect due to differences in the charge distribution of protons.[14,21] This isotope shift is wavelength dependent. For the 834.682 nm line of Xe I $(6S'[1/2]1 \rightarrow 6P'[3/2]1)$, Suzuki *et al.*[13] provide all isotope shifts; their study also reports shifts associated with several other lines in the 820.6 to 904.5 nm-air range. Additionally, xenon isotopes vary in their relative natural abundances.[14] We account for this effect by normalizing each set of isotope lines by unity prior to scaling them by natural abundance. Figure 4 illustrates frequency shifting of σ^- lines of ^{129}Xe and ^{131}Xe. For the sake of completeness, we also report the full σ^+ spectrum of the two isotopes in Fig. 5.

B. Transition line spectra modeling of isotopes with zero nuclear spin

For the treatment of the remaining seven even-mass isotopes (^{124}Xe, ^{126}Xe, ^{128}Xe, ^{130}Xe, ^{132}Xe, ^{134}Xe, and ^{136}Xe with $I=0$), we use the simpler anomalous Zeeman theory. Once all possible M_J values are generated from Eq. (2.1), transition energies are determined from Eq. (2.2); owing to the dependence of energy displacements on H and M_J alone, line components of all these isotopes have equal transition energies. Intensity formulas given in Eq. (2.3) are applied prior to isotope shifting[13] and scaling[14] of the lines plotted in Fig. 6; this latter step is identical to the treatment of ^{129}Xe and ^{131}Xe outlined at the end of Sec. IV A.

C. Natural and Doppler broadening of line spectra

Lastly, we apply a Voigt profile[4] to the overall spectrum combining line components associated with each isotope. It suffices, here, to briefly describe such a profile as the product

TABLE V. Illustration of the calculation of transition intensities based on σ^- components of the $6S'[1/2]1 \rightarrow 6P'[3/2]1$ line of Xe I when $H=312$ G.

Transition	Energy (GHz)	I_N	I	$N_M^{J,F}$	$N_{M'}^{J+1,F'}$
$\langle 1\|4\rangle$	−0.374	2	$(4X^{1,3/2}_{1,1/2}Y^{2,5/2}_{0,1/2})^2$	$2(X^{1,3/2}_{1,1/2})^2$	$4(Y^{2,5/2}_{0,1/2})^2$
$\langle 1\|5\rangle$	6.99	2	$(4X^{1,3/2}_{1,1/2}Y^{2,3/2}_{0,1/2})^2$	$2(X^{1,3/2}_{1,1/2})^2$	$4(Y^{2,3/2}_{0,1/2})^2$
$\langle 2\|6\rangle$	−0.398	3.74	$(6X^{1,3/2}_{0,1/2}Y^{2,5/2}_{-1,1/2}+4X^{1,3/2}_{1,-1/2}Y^{2,5/2}_{0,-1/2})^2$	$(X^{1,3/2}_{0,1/2})^2+2(X^{1,3/2}_{1,-1/2})^2$	$6(Y^{2,5/2}_{-1,1/2})^2+4(Y^{2,5/2}_{0,-1/2})^2$
$\langle 2\|7\rangle$	6.75	1.04	$(6X^{1,3/2}_{0,1/2}Y^{2,3/2}_{-1,1/2}+4X^{1,3/2}_{1,-1/2}Y^{2,3/2}_{0,-1/2})^2$	$(X^{1,3/2}_{0,1/2})^2+2(X^{1,3/2}_{1,-1/2})^2$	$6(Y^{2,3/2}_{-1,1/2})^2+4(Y^{2,3/2}_{0,-1/2})^2$
$\langle 3\|6\rangle$	−9.32	3.77×10^{-5}	$(6X^{1,1/2}_{0,1/2}Y^{2,5/2}_{-1,1/2}+4X^{1,1/2}_{1,-1/2}Y^{2,5/2}_{0,-1/2})^2$	$(X^{1,1/2}_{0,1/2})^2+2(X^{1,1/2}_{1,-1/2})^2$	$6(Y^{2,5/2}_{-1,1/2})^2+4(Y^{2,5/2}_{0,-1/2})^2$
$\langle 3\|7\rangle$	−2.17	3.22	$(6X^{1,1/2}_{0,1/2}Y^{2,3/2}_{-1,1/2}+4X^{1,1/2}_{1,-1/2}Y^{2,3/2}_{0,-1/2})^2$	$(X^{1,1/2}_{0,1/2})^2+2(X^{1,1/2}_{1,-1/2})^2$	$6(Y^{2,3/2}_{-1,1/2})^2+4(Y^{2,3/2}_{0,-1/2})^2$
$\langle 4\|8\rangle$	−0.426	7.35	$(24X^{1,3/2}_{-1,1/2}Y^{2,5/2}_{-2,1/2}+6X^{1,3/2}_{0,-1/2}Y^{2,5/2}_{-1,-1/2})^2$	$2(X^{1,3/2}_{-1,1/2})^2+(X^{1,3/2}_{0,-1/2})^2$	$24(Y^{2,5/2}_{-2,1/2})^2+6(Y^{2,5/2}_{-1,-1/2})^2$
$\langle 4\|9\rangle$	6.51	0.836	$(24X^{1,3/2}_{-1,1/2}Y^{2,3/2}_{-2,1/2}+6X^{1,3/2}_{0,-1/2}Y^{2,3/2}_{-1,-1/2})^2$	$2(X^{1,3/2}_{-1,1/2})^2+(X^{1,3/2}_{0,-1/2})^2$	$24(Y^{2,3/2}_{-2,1/2})^2+6(Y^{2,3/2}_{-1,-1/2})^2$
$\langle 5\|8\rangle$	−8.96	7.27×10^{-5}	$(24X^{1,1/2}_{-1,1/2}Y^{2,5/2}_{-2,1/2}+6X^{1,1/2}_{0,-1/2}Y^{2,5/2}_{-1,-1/2})^2$	$2(X^{1,1/2}_{-1,1/2})^2+(X^{1,1/2}_{0,-1/2})^2$	$24(Y^{2,5/2}_{-2,1/2})^2+6(Y^{2,5/2}_{-1,-1/2})^2$
$\langle 5\|9\rangle$	−2.02	9.82	$(24X^{1,1/2}_{-1,1/2}Y^{2,3/2}_{-2,1/2}+6X^{1,1/2}_{0,-1/2}Y^{2,3/2}_{-1,-1/2})^2$	$2(X^{1,1/2}_{-1,1/2})^2+(X^{1,1/2}_{0,-1/2})^2$	$24(Y^{2,3/2}_{-2,1/2})^2+6(Y^{2,3/2}_{-1,-1/2})^2$
$\langle 6\|10\rangle$	−0.460	12	$(24X^{1,3/2}_{-1,-1/2}Y^{2,5/2}_{-2,-1/2}$	$2(X^{1,3/2}_{-1,-1/2})^2$	$24(Y^{2,5/2}_{-2,-1/2})^2$

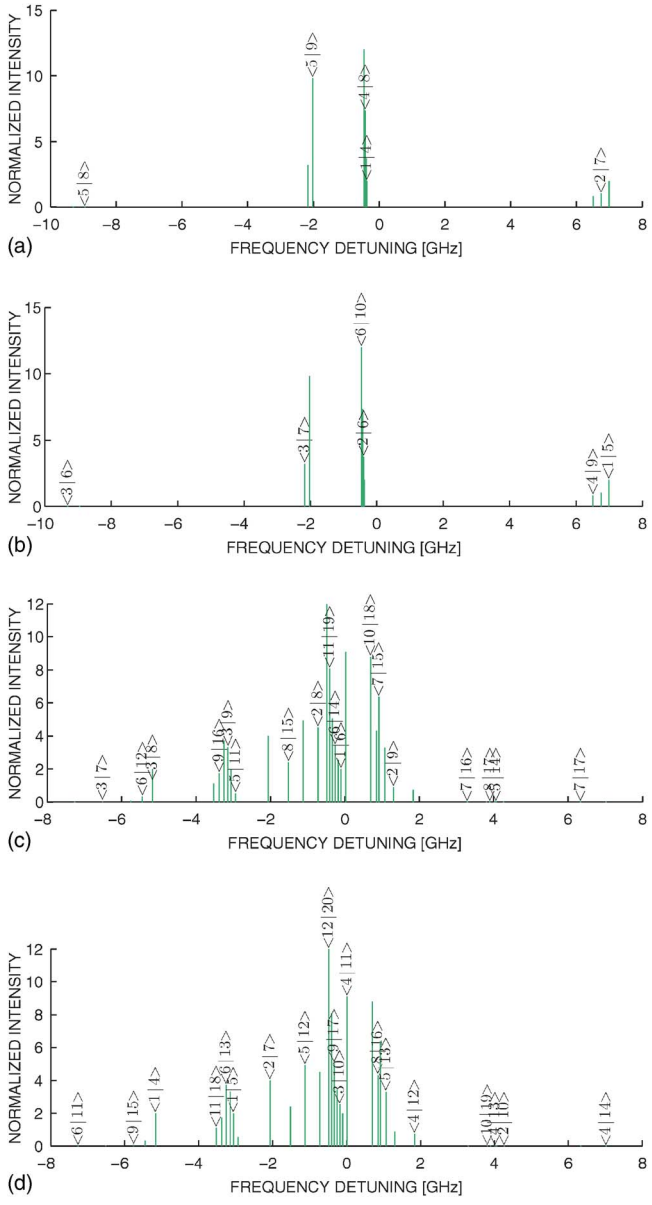

FIG. 2. (Color online) σ^- transition line spectra of ^{129}Xe and ^{131}Xe for an external field strength of 312 G. For the sake of clarity, annotations are applied to every other line. (a) ^{129}Xe line spectrum. (b) ^{129}Xe line spectrum. (c) ^{131}Xe line spectrum. (d) ^{131}Xe line spectrum

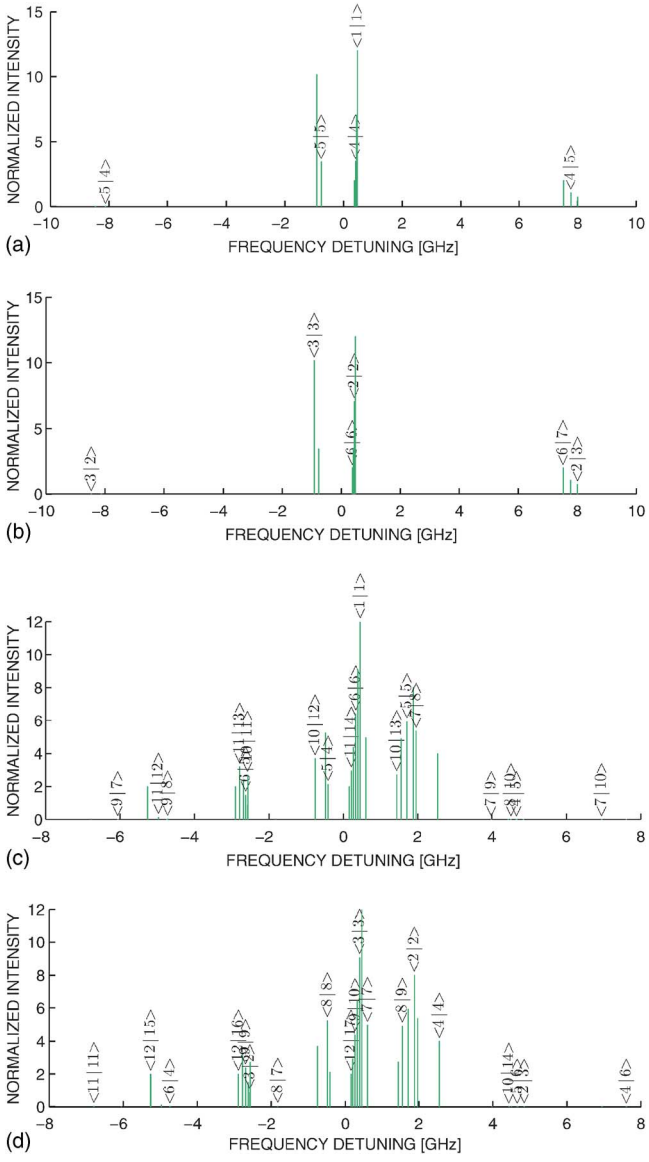

FIG. 3. (Color online) σ^+ transition line spectra of ^{129}Xe and ^{131}Xe for an external field strength of 312 G. For the sake of clarity, annotations are applied to every other line. (a) ^{129}Xe line spectrum. (b) ^{129}Xe line spectrum. (c) ^{131}Xe line spectrum. (d) ^{131}Xe line spectrum.

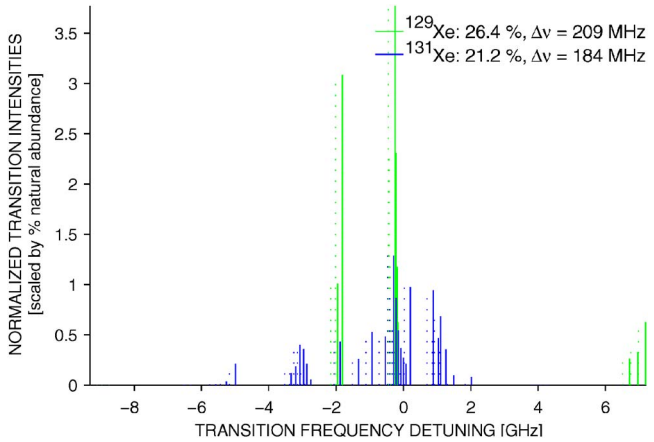

FIG. 4. (Color online) σ^- transition line strengths of ^{129}Xe and ^{131}Xe for an external field strength of 312 G. The figure further illustrates the frequency shift associated with each isotope (unshifted lines are dashed).

of a two-step process.[22,23] In the first, a "cold spectrum" is generated by Lorentz-broadening the lines. This is achieved through a Lorentz distribution simulating spontaneous emission of light through a rate $\Delta\nu=A_{ij}/(2\pi)$, which represents the width at half-maximum of the distribution and is proportional to a transition constant A_{ij}, whose value is reported by Miller *et al.*[24] for the 834.682 nm Xe I line. In the second, the cold spectrum is convolved with a Doppler distribution to generate a "warm spectrum" that simulates the absorption spectrum of Xe I for a particular external magnetic field strength and plasma kinetic temperature. An illustration of the broadening process is shown in Fig. 7 in which line, cold, and warm spectra are overlaid.

V. SOLVING FOR MAGNETIC FIELD STRENGTHS AND PLASMA KINETIC TEMPERATURES FROM XE I ABSORPTION SPECTRA

A. Experimental setup for xenon optogalvanic cell spectroscopy

We used spectral data from a galvatron (also known as optogalvanic cell) to validate the nonlinear ZHFS model and used a commercial least-squares solver, LSQNONLIN,[25] in computing magnetic field strengths and kinetic temperatures.

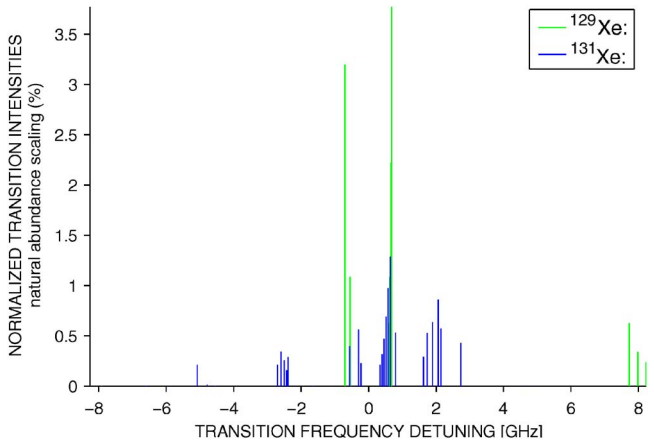

FIG. 5. (Color online) σ^+ transition line strengths of ^{129}Xe and ^{131}Xe (isotope shifts are accounted for).

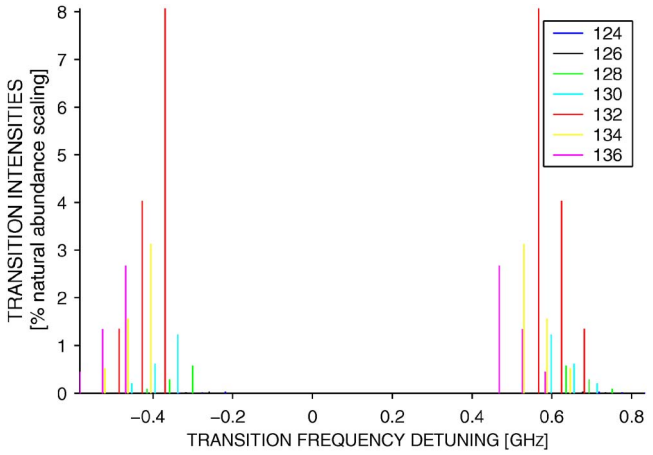

FIG. 6. (Color online) Line spectrum of xenon isotopes with no nuclear spin.

Smith *et al.*[26] describe the experiment in detail. The galvatron consists of a glass tube filled with xenon and neon (nonreacting filler). It encloses two electrodes for plasma breakdown with 250 V potential difference applied between them. When the plasma is excited by a light source tuned to a particular transition's wavelength, the discharge current varies proportionally with the radiative absorption intensity of the plasma.

The light source consists of a tunable single-mode diode-laser centered at 834.682 nm with a 10 GHz mode-hop-free frequency detuning range. A 2 GHz free-spectral-range (FSR) Fabry-Perot interferometer ensures high-resolution measurements of the detuning. A pair of Helmholtz coils, on either side of the galvatron, produce field lines perpendicular to the galvatron's axis and of maximum intensity at its center. To excite σ-transitions, the polarization vector of the laser beam is rotated until perpendicular to the magnetic field direction inside the galvatron. A lock-in amplifier operating with a time-constant of 300 ms reads discharge current variations, relays them to a PC, and controls the voltage of the laser's piezoelectric tuning element.

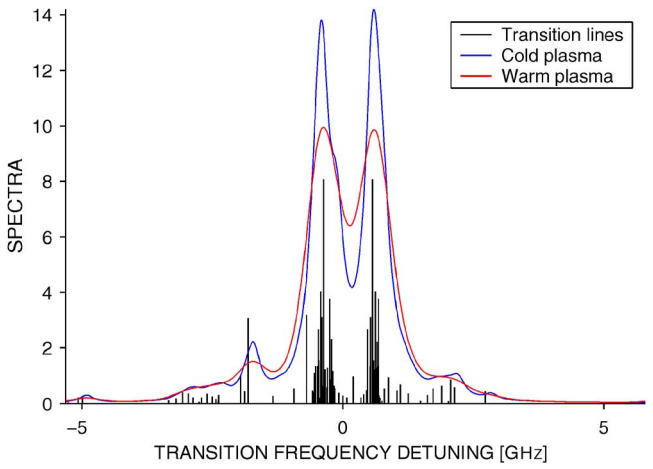

FIG. 7. (Color online) Voigt profile generation from the spectrum of transition lines. The normalized cold and warm spectra shown are based on Lorentz and Doppler broadenings of transition lines. The external field strength is 312 G in this plot. As shown, normalized line intensities were amplified by a factor of 20 for the sake of illustration.

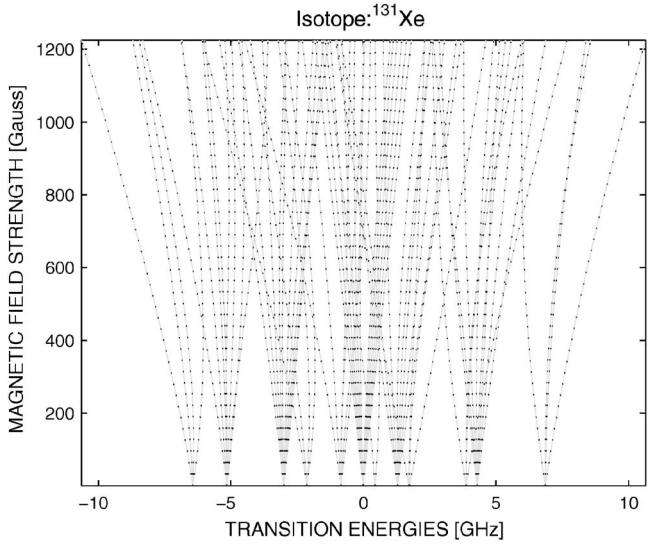

FIG. 8. Variation of transition energies of ^{131}Xe with magnetic field strength.

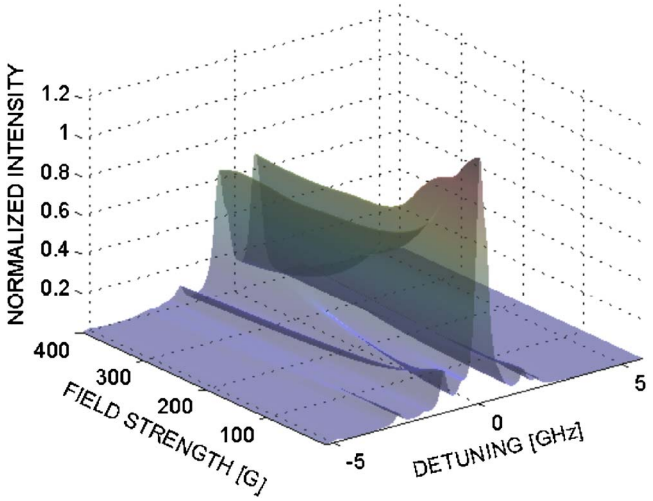

FIG. 9. (Color online) Surface plot illustrating a smooth variation of cold spectra with magnetic field strength.

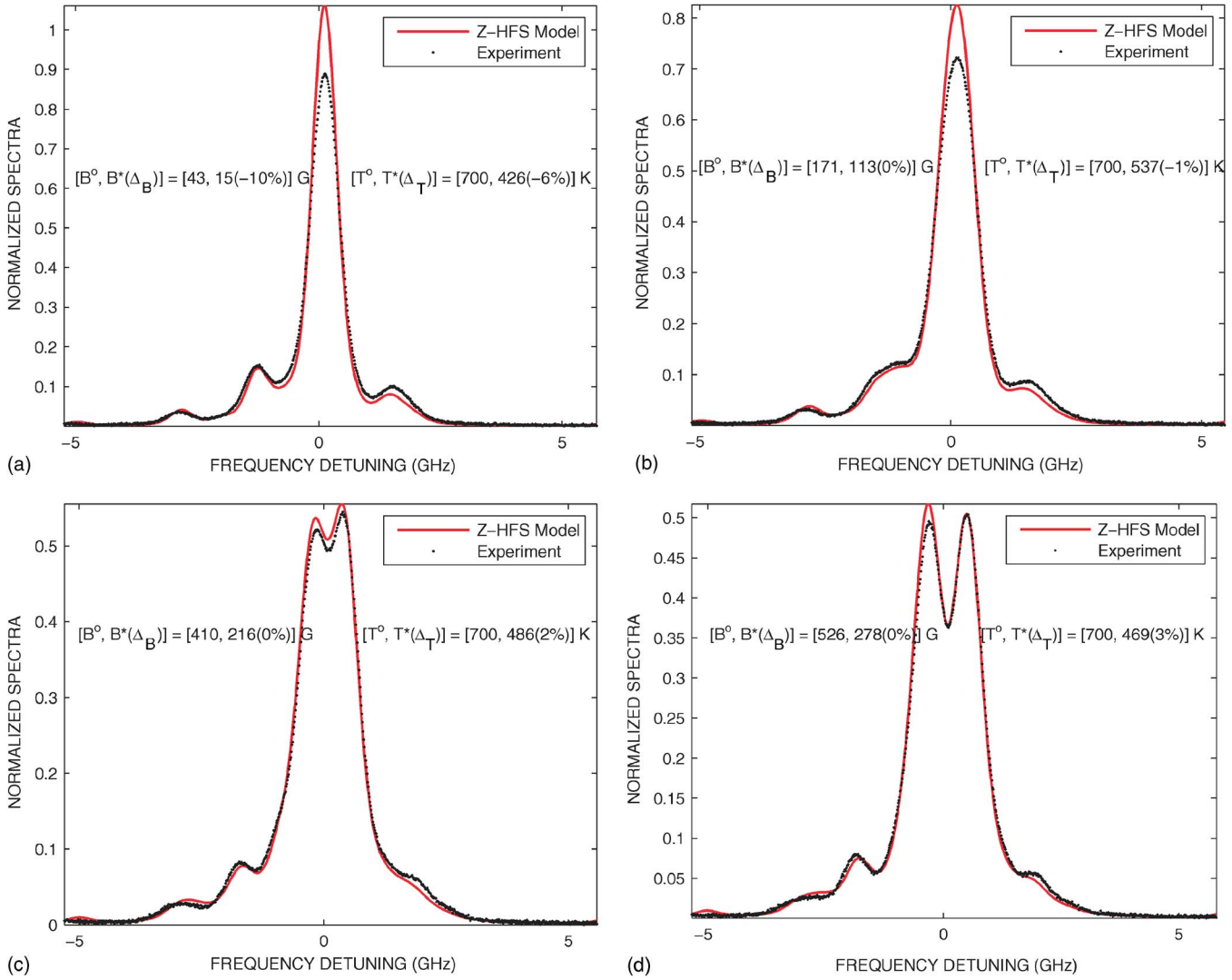

FIG. 10. (Color online) Least-squares fitting of neutral xenon absorption spectra at 834.682 nm in an optogalvanic cell at various external magnetic field strength settings. The fitting is based on optimal magnetic field strength and plasma kinetic temperature outputted by Matlab's LSQNONLIN solver. (a) 30 G external field strength setting. (b) 120 G external field strength setting. (c) 210 G external field strength setting. (d) 270 G external field strength setting.

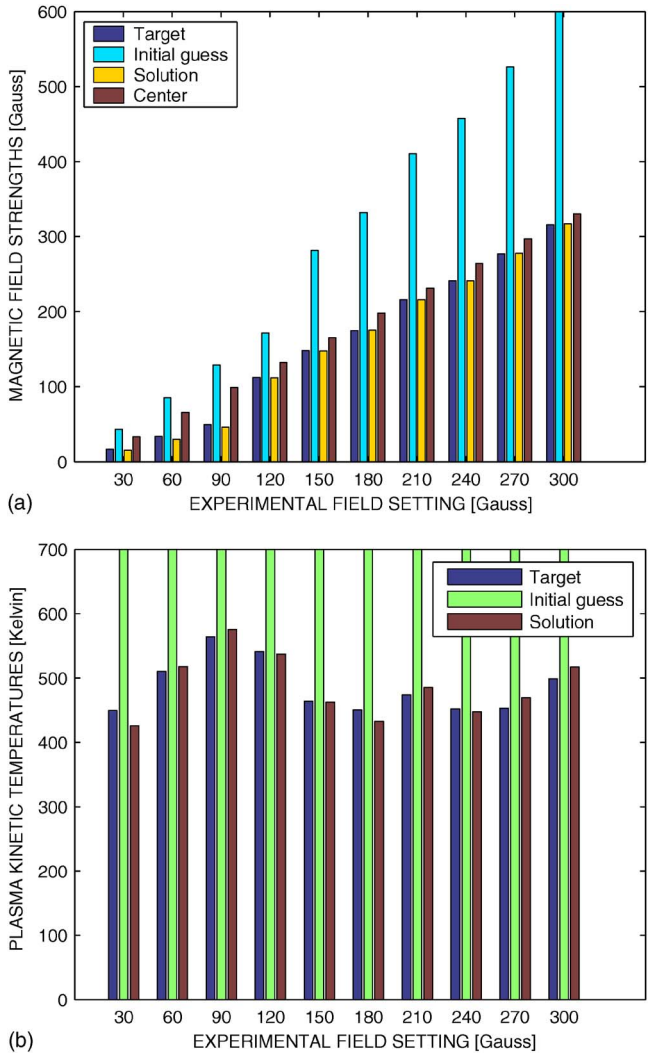

FIG. 11. (Color online) Comparison of solver solutions with target values, center-field values (applicable to field strength solutions only), and initial guesses. (a) External magnetic field strength solutions. (b) Plasma kinetic temperature solutions.

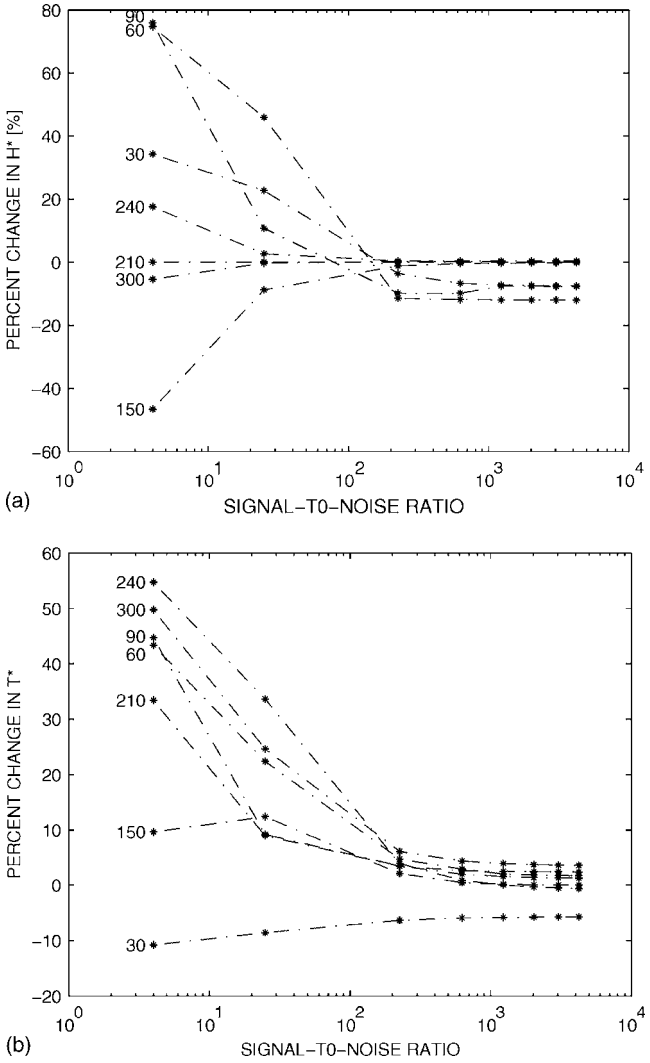

FIG. 12. Effect of signal-to-noise ratio (SNR) on the calculation of external magnetic field strength (H) and plasma kinetic temperature (T) based on nonlinear least-squares fitting of neutral xenon absorption spectra at 834.682 nm-air. Gaussian noise was added to experimental absorption spectra. (a) Effect of SNR on H convergence. (b) Effect of SNR on T convergence.

The experiment was conducted at ten field strength settings within an interval spanning 30 to 300 G in 30 G increments. A Hall-effect probe placed 3 cm above the galvatron's symmetry axis, coinciding with its interrogation volume, confirmed the settings. According to the probe's calibration runs, this translated to 1% higher "center-field strengths" along the symmetry axis.

B. Continuity of transition energies and smooth distribution of absorption spectra

Successful application of LSQNONLIN requires a smooth and continuous input error function. A study of the evolution of energy levels with magnetic field strength confirmed their continuity. With machine tolerance being the only constraint, we found the range of magnetic field strengths recoverable with this technique to extend from 0.01 to 50 000 G; we stress, however, that the nonlinear ZHFS model is theoretically applicable to an arbitrarily wide range of field strengths. Figure 8 illustrates continuous variations of transition energies from 0.01 to 1000 G for ^{131}Xe. Energy level continuity led to a smooth evolution of Xe I cold spectra with magnetic field strength as revealed by the surface plot of Fig. 9.

C. Computing magnetic field strengths and plasma kinetic temperature from optogalvanic spectra

Prior to applying LSQNONLIN to solve for external field strength on the plasma and kinetic temperature, we first set out to find what "target" magnetic field strengths and kinetic temperatures and "optimal" physical parameters best model the 834.682 nm absorption line; these variables were simultaneously solved for. To account for any potential contamination of the external magnetic field by devices surrounding the galvatron (such as the Fabry-Perot interferometer) and the plasma-induced magnetic field as well as any possible errors associated with Hall probe measurements, we solved for effective (target) field strengths felt by xenon neutrals at the various experimental settings. Center-field strength values were used as starting guesses and error

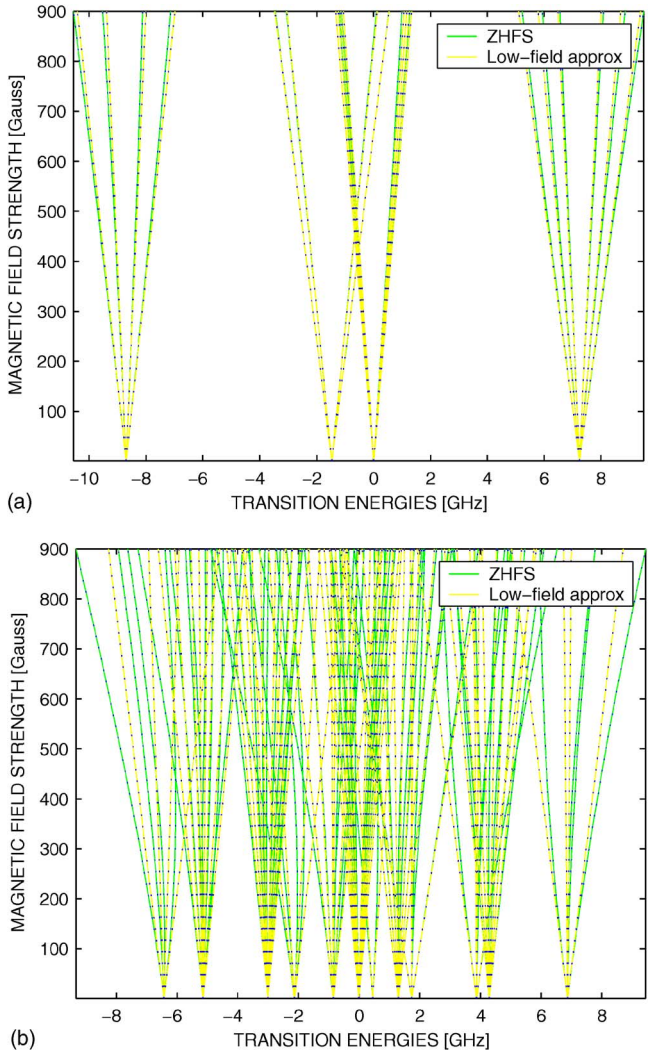

FIG. 13. (Color online) Variation of transition energies of ^{129}Xe and ^{131}Xe as predicted by weak-field linear and nonlinear theories of the Zeeman effect of hyperfine structure. (a) Transition energies of ^{129}Xe. (b) Transition energies of ^{131}Xe.

bounds were set arbitrarily wide at $\pm 100\%$ about them. As for target temperatures, they were computed based on a starting guess of 700 K and an error bound interval of 300 K. We inferred this width by correlating our galvatron's discharge voltage setting with that of a previous optogalvanic study,[27] which reported a kinetic temperature of 800 K at a 440 V discharge voltage setting. Due to uncertainties associated with physical parameters[28] involved in modeling the 834.682 nm line, we also needed to determine what optimal values would minimize the error, ϵ, between experimental and simulated spectra within their respective published error bounds. Published mean values served as initial guesses to the solver.

Having determined target solutions and optimal physical parameters, we set out to test the performance of the solver in recovering field strengths and kinetic temperatures when initial guesses significantly deviated from center and target values. As the good fits of optogalvanic spectra plotted in Fig. 10 imply, LSQNONLIN was successful in simultaneously determining the strengths of the external magnetic field and its kinetic temperature. These reveal convergences

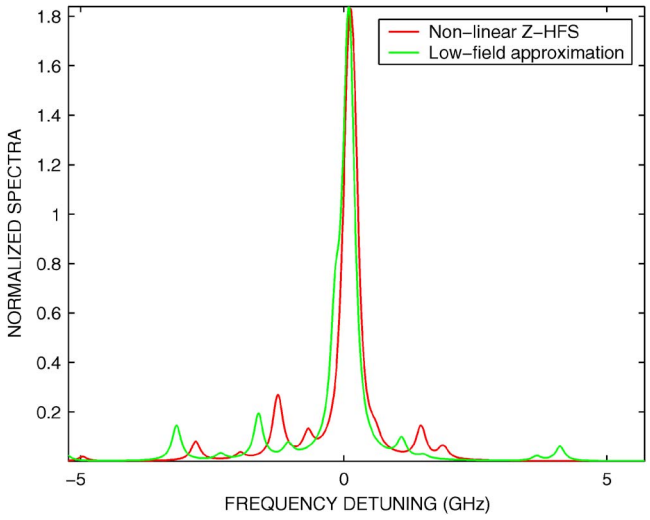

FIG. 14. (Color online) Comparison of cold spectra as computed by nonlinear and weak-field Zeeman effects of hyperfine structure at 17 G.

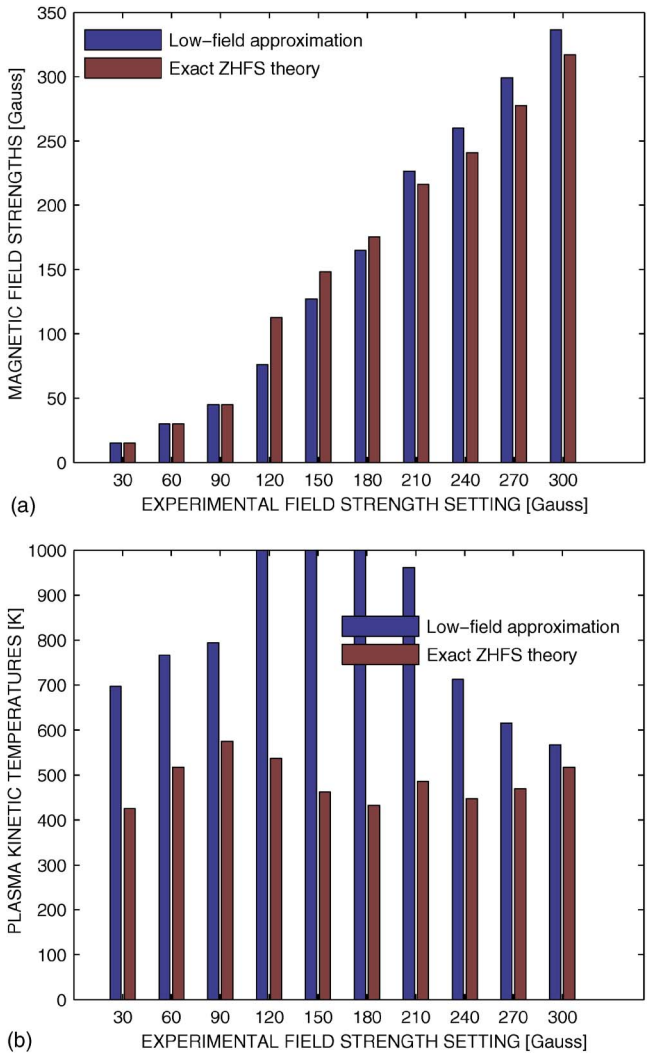

FIG. 15. (Color online) Comparison of LSQNONLIN's solution outputs based on the weak-field linear and nonlinear theories of the Zeeman effect of hyperfine structure. (a) External magnetic field strength solutions. (b) Plasma kinetic temperature solutions.

TABLE VI. Solution outputs from the application LSQNONLIN to the determination of optimal physical parameters and target magnetic field strengths and kinetic temperatures based on Xe I absorption spectra about 834.682 nm at ten external magnetic field settings.

						Magnetic field strengths (G)						
Center		33.19	65.6	99.01	131.9	164.8	197.8	230.8	263.7	296.7	329.7	
Optimal		16.59	33.68	49.51	112.1	148.1	174.6	216	240.8	277	315.6	
States	Isotopes					Optimal variables						Averages
						Galvatron temperatures (K)						
		450	510.8	563.9	540.9	464.2	450.7	474.3	452.2	453.5	499.1	486
						Isotope shifts (MHz) - relative to 136						
	124	250.3	250.2	250.2	250.2	250.2	250.2	250.2	250.2	250.2	250.2	250.2
	126	209.1	209.1	209.1	209.1	209.1	209.1	209.1	209.1	209.1	209.1	209.1
	128	167.9	167.9	167.9	167.9	167.9	167.9	167.9	167.9	167.9	167.9	167.9
	129	208.7	208.7	208.7	208.7	208.7	208.7	208.7	208.7	208.7	208.7	208.7
	130	130.4	130.4	130.4	130.4	130.4	130.4	130.4	130.4	130.4	130.4	130.4
	131	183.6	183.6	183.6	183.6	183.6	183.6	183.6	183.6	183.6	183.6	183.6
	132	98.9	98.9	98.9	98.9	98.9	98.9	98.9	98.9	98.9	98.9	98.9
	134	62.9	62.9	62.9	62.9	62.9	62.9	62.9	62.9	62.9	62.9	62.9
						Hyperfine constants (MHz)						
$6S'[1/2]1$	129	−5811	−5811	−5786	−5811	−5797	−5786	−5811	−5811	−5811	−5811	−5805
	131	−2893	−2899	−2899	−2898	−2899	−2899	−2889	−2899	−2886	−2886	−2895
$6P'[3/2]1$	129	1718	1718	1718	1718	1718	1718	1718	1718	1718	1718	1718
	131	855.8	855.8	855.8	855.8	855.8	855.8	855.8	855.8	855.8	855.8	855.8
		Electron Landé g-factors: g_J										
$6S'[1/2]1$		1.321	1.321	1.321	1.321	1.321	1.321	1.321	1.321	1.321	1.321	1.321
$6P'[3/2]1$		1.189	1.189	1.189	1.191	1.191	1.191	1.191	1.191	1.191	1.191	1.19
		Nuclear moments: μ_N										
	129	−0.7767	−0.7767	−0.7767	−0.7767	−0.7767	−0.7767	−0.7767	−0.7767	−0.7769	−0.7769	−0.7767
	131	0.7498	0.7498	0.7498	0.7498	0.7498	0.7498	0.7498	0.7498	0.7498	0.7498	0.7498
						Einstein emission coefficient						
		0.8743	0.8904	0.8904	0.8904	0.8904	0.8904	0.8904	0.8904	0.8904	0.8904	0.8888

to within 10% of target temperatures and field intensities even when starting guesses deviated by as much as 100% from expected targets. Values for the starting guesses H_o and T_o, solutions H^* and T^*, and deviations ΔT and ΔH are listed in each plot. The latter two parameters are deviations of solutions from target parameters that indicate the quality of the convergence; the smaller the deviations, the better the match between solutions and corresponding targets. Figure 11(a) provides a complete summary of solutions, target values, starting guesses, and center-field strengths at all ten experimental settings. As shown in the figure, solutions remain consistently close to target values at all settings but deviate from center-field values by as much as 50% below 100 G.

In the event that the level of field contamination from surrounding devices (such as the Fabry-Perot interferometer) and errors from Hall-probe calibration were insignificant; that is, if measured center-field strengths effectively acted upon xenon species, the previously mentioned mismatch would suggest a weakness of the spectral model at field settings below 100 G that could be attributed to three reasons. First, the nonlinear ZHFS model does not account for the electric quadrupole interaction between nuclei and respective electron clouds arising from the former particles' asymmetric structure[12] (recall discussion at the end of Sec. IV A). Second, the magnitudes of the Zeeman splitting of some hyperfine energy levels approach our solver's numerical tolerance levels as the field strength drops below 100 G. Lastly, Doppler broadening further amplifies the problem by causing a blurring of line spectra.

Kinetic temperature solutions, on the other hand, remained close to targets independently of the magnetic field strength. The relatively flat distribution of solutions shown in Fig. 11(b) illustrates this fact and validates the solver's reliability in computing plasma kinetic temperature given that the galvatron's discharge voltage was kept constant throughout the data acquisition process.

D. Sensitivity of solver to signal-to-noise ratio (SNR)

Though the above analysis dealt with optogalvanic spectra, the primary purpose of the solver is to resolve magnetic field strengths and kinetic temperatures from laser-induced fluorescence spectra (from future work) of electric thruster discharges. The latter spectra are typically noisier with SNR

levels less than 100.[22] Hence, to further validate the H and T solver, we studied the effect of noise on convergence. Gaussian noise, at various SNR levels, was added to optogalvanic spectra. This study revealed little impact of noise on the quality of convergence for SNR levels above 200. At lower SNR levels (about 20), deviations of solutions from expected target solutions still remained below 50% at all field strength settings investigated. Figures 12(a) and 12(b) respectively illustrate the evolution of the temperature and field strength deviations with decreasing SNR.

VI. NECESSITY OF THE NONLINEAR ZEEMAN THEORY OF HYPERFINE STRUCTURE FOR XE I LINE SHAPE MODELING

For the sake of completeness, we compare the performance of the nonlinear ZHFS theory with its weak-field linear counterpart. In our analysis, we pay particular interest to the range of field strengths investigated (0 to 300 G) by comparing the variations of transition energies with magnetic field strength as predicted by the two theories for the two xenon isotope with nonzero nuclear spins. From Fig. 13(a), we find that, for the case of ^{129}Xe with a small nuclear spin, both theories agree well beyond the upper bound of our range of interest. But, for the case of ^{131}Xe whose nuclear spin is higher—implying a more complex hyperfine structure—Fig. 13(a) reveals a greater nonlinearity of the variation of transition energies; hence the larger disparities between the predictions of the two models. The differences become noticeable from 100 G and intensify from 0.1 GHz to 1 GHz as the field strength increases from 300 G to 900 G (see line components centered about -6.5 GHz and -2 GHz, for example).

The above analysis suggests that the weak-field approximation is reliable for locating energies of Xe I transition lines about 834.682 nm provided that the field strength does not exceed 300 G. Does the same apply to line intensities? For the sake of clarity, we chose to answer this question using cold spectra instead of cluttered transition line plots; from Fig. 14, we note clear differences between cold spectra modeled from the two theories for an external field setting as low as 17 G. Furthermore, we tested the performance of a magnetic field strength solver based on the low-field approximation; Figs. 15(a) and 15(b) compare the latter solver's solutions with those reported in Sec. V C. The implementation of LSQNONLIN based on the linear model revealed a good match of field strength solutions only below 90 G [see Fig. 15(a)]. Above 90 G, the solutions deviate by as much as 30% from those outputted by the nonlinear ZHFS solver. Worse, a comparison of plasma kinetic temperature solutions shown in Fig. 15(b) reveals no match throughout the range of field strengths investigated. Assuming that the mean of temperature solutions (on the order of 500 K) obtained from the nonlinear ZHFS theory is accurate, we conclude that the weak field theory is not reliable for the prediction of plasma kinetic temperatures from Xe I spectra.

This comparative analysis omits the strong-field linear approximation since its range of applicability, spanning 10 to 20 KG,[9] is far beyond the range investigated in this study.

VII. CONCLUSION

We successfully applied theories of the linear Anomalous Anomalous Zeeman effect and the nonlinear Zeeman effect of hyperfine structure on even- and odd-mass isotopes, respectively, to simulate neutral xenon absorption spectra in the plasma environment of an optogalvanic cell to which an external magnetic field was applied. The reliability of the model prompted us to use it as an input function to a nonlinear least-squares solver of external magnetic field strengths and plasma kinetic temperatures based on optimal fitting of experimental spectra. We noted good convergence of the solver in both variables even in the presence of Gaussian noise. The results reported in this study reveal that the solver is a reliable computational tool for the study of the interaction between an external magnetic field and a xenon plasma and the extraction of Maxwellian velocity distributions of neutral xenon atoms in Hall thruster plumes.

ACKNOWLEDGMENTS

This research project is funded by Air Force Office of Scientific Research Grant No. F49620-02-1-0051 monitored by Dr. Mitat Birkan. We thank all other PEPL members as well as UM's body of students and staff for their committed efforts in keeping the establishment on its traditional path of academic and scientific progress; in particular, we are grateful to graduate student Serge S. Badiane for his valuable assistance with MatLab during the evolution of this project.

[1] P. Y. Peterson, A. D. Gallimore, and J. M. Haas, 27th International Electric Propulsion Conference, Pasadena, CA, 2001.
[2] W. A. Hargus, Jr., Ph.D. thesis, Stanford University, 2001.
[3] R. R. Hofer and A. D. Gallimore, 38th Joint AIAA Propulsion Conference, Indianapolis, IN, 2002.
[4] H. Haken and H. C. Wolf, *The Physics of Atoms and Quanta*, 7th ed. (Springer-Verlag, Berlin, 1997).
[5] I. I. Sobelman, *Atomic Spectra and Radiative Transitions*, 2nd ed. (Springer-Verlag, New York, 1992).
[6] C. G. Darwin, Proc. R. Soc. London, Ser. A **115**, 1 (1927).
[7] K. Darwin, Proc. R. Soc. London, Ser. A **118**, 264 (1928).
[8] R. F. Bacher, Ph.D. thesis, University of Michigan, 1930.
[9] R. H. Garstang, Rep. Prog. Phys. **40**, 105 (1977).
[10] Interpretation of M: While M is a valid quantum number in the low-field approximation, it is not considered one in the nonlinear Zeeman theory on hyperfine structure. Its use in the latter theory is exclusively limited to denote possible sums of M_J and M_I and to insure conservation of angular momentum.
[11] http://physics.nist.gov/Pubs/AtSpec/node09.htmlnode095.
[12] S. Svanberg, *Atomic and Molecular Spectroscopy: Basic Aspects and Practical Applications*, 3rd ed. (Springer-Verlag, New York, 2001).
[13] M. Suzuki, K. Katoh, and N. Nishimiya, Spectrochim. Acta, Part A **58**, 2519 (2002).
[14] R. B. Firestone and C. M. Baglin, *Table of Isotopes* (Wiley, New York, 1999).
[15] E. B. Saloman, Energy levels and observed spectral lines of xenon, Xe I through Xe LIV, Technical report, 2004.
[16] J. Emsley, *The Elements* (Oxford U. P., New York, 1995).
[17] D. A. Jackson and M. C. Coulombe, Proc. R. Soc. London, Ser. A **327**, 137 (1972).
[18] http://physics.nist.gov/PhysRefData/ASD/lines_form.html.
[19] The physical parameters (e.g., hyperfine structure constant and Landé g-factors) used to write the eigenvalue problem slightly differ from nominal published values. These values are optimal within their associated ranges of uncertainty (refer to Sec. V C outlining how they were found).
[20] Bacher (Refonly reports intensity formulas for $J \rightarrow J-1$ transitions. However, for the 834.682 nm line, respective upper and lower J values are 1

and 2; hence, falling in the class of to $J \rightarrow J+1$ transitions. To appropriately account for this class of transitions, one simply needs switching upper by lower states in the intensity formulas as suggested by Bacher.
[21]T. B. Smith, Ph.D. thesis, University of Michigan, 2003.
[22]T. B. Smith, D. A. Herman, A. D. Gallimore, and R. P. Drake, 27th International Electric Propulsion Conference, Pasadena, CA, 2001.
[23]W. A. Hargus, Jr. and M. A. Capelli, Appl. Phys. B: Lasers Opt. **72**, 961 (2001).
[24]M. H. Miller, R. A. Roig, and R. D. Bengtson, Phys. Rev. A **8**, 480 (1973).
[25]LSQNONLIN is commercial nonlinear least-squares solver within MATLAB©, Version 6.5, Release 13.
[26]T. B. Smith, W. Huang, and B. B. Ngom, 30th International Electric Propulsion Conference, Florence, Italy, 2007.
[27]G. J. Williams, Jr., Ph.D. thesis, University of Michigan, 2000.
[28]Uncertainties on physical parameters: Some physical parameters were published with rather substantial uncertainties. For example, the published value of the spontaneous emission coefficient involved in the 834.682 nm transition of neutral xenon is only accurate to within 40%.